

Beam Control and a New Laboratory Testbed for Adaptive Optics in a Maritime Environment

Capt Melissa S. Corley, Masaki Nagashima, Brij N. Agrawal
 Naval Postgraduate School
 Monterey, CA 93943

505-217-4148, 831-656-2808, 831-656-3338

melissa.corley@us.af.mil, mnagashi@nps.edu, agrawal@nps.edu

Abstract—The Naval Postgraduate School is developing a laboratory environment for testing advanced beam control methods for compensation of atmospheric turbulence in adaptive optics for use in a maritime environment. This paper presents a multichannel transverse adaptive filter for beam control. Adaptive filters are useful for such control due to the constantly changing nature of atmospheric turbulence. A multichannel filter is required due to the multiple deformable mirror input commands and wavefront sensor output measurements in the system. The filter is augmented with an integrated bias estimator. Additionally, this paper describes a method for generating horizontal-like atmospheric turbulence by using two liquid crystal spatial light modulators. The development and components of the new laboratory testbed are described, and preliminary simulation results are presented.¹²

and slant path turbulence present a more difficult and less well understood problem than the vertical and near-vertical turbulence paths used for astronomical adaptive optics. As such, current research is underway to develop a testbed for developing beam control methods in the presence of a thick aberrator that will approximate horizontal turbulence.

The Technique of Adaptive Optics

Adaptive optics (AO) is useful in correcting for aberrations in imaging and communications systems caused by turbulence or other disturbances in the propagation medium. A typical adaptive optics system is shown in Figure 1. The three primary components of an AO system are a wavefront sensor to determine how the beam is distorted, a control computer to calculate the correction to be applied, and a corrective element, usually a deformable mirror (DM), to implement the applied commands [7].

TABLE OF CONTENTS

1. INTRODUCTION.....	1
2. ADAPTIVE FILTER.....	2
3. TURBULENCE SIMULATOR.....	6
4. LABORATORY TESTBED.....	7
5. SIMULATION.....	9
6. CONCLUSIONS.....	11
7. ACKNOWLEDGEMENTS.....	12
REFERENCES.....	12
BIOGRAPHY.....	13

1. INTRODUCTION

The Naval Postgraduate School is developing a laboratory environment for testing advanced beam control methods for compensation of atmospheric turbulence in adaptive optics. Previous adaptive optics work at the NPS has been applied primarily to vibration control and segment alignment for space telescopes and segmented mirror systems [1], [2]. The use of robust control has been explored with segmented mirror systems as well [2]. Adaptive filters have been used by the NPS in the control of optical beam jitter [3], [4], but this is the first time they will be used by the NPS for compensation of atmospheric turbulence. However, UCLA and the Starfire Optical Range have used multichannel filters in astronomical adaptive optics systems [5], [6].

Maritime beam control for shipboard applications and high energy lasers is of great interest to the Navy. Horizontal

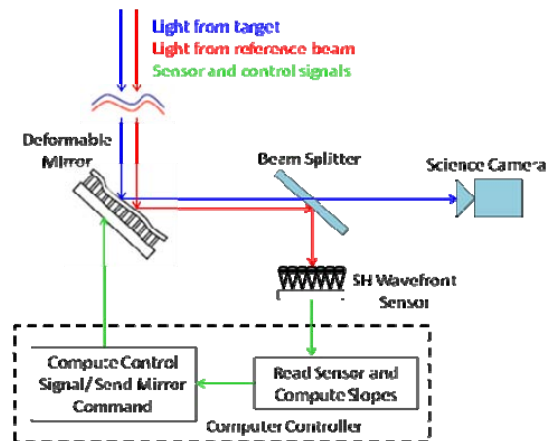


Figure 1 – Typical adaptive optics system with SH WFS

In this system, a reference beam that sees the same disturbance as the target is sent to the wavefront sensor. A Shack-Hartmann (SH) wavefront sensor (WFS) is an array of lenslets which produces a grid pattern of spots on a detector. An ideal wavefront is flat, producing a known grid pattern, while an aberrated wavefront will produce some x and y offsets from the reference grid. Thus, the sensor measures x and y positions on the detector and the computer determines the slope of the wavefront from the offsets. Figure 2 shows a schematic of a SH WFS.

The control computer uses the slope error from the sensor to determine what commands to send to the deformable mirror to correct for the error. Finally, the mirror deforms

¹ U.S. Government work not protected by U.S. copyright.
² IEEEAC paper #1534, Version 1, Updated April 14, 2009.

according to the received commands and the process repeats, actively correcting for the changing turbulence.

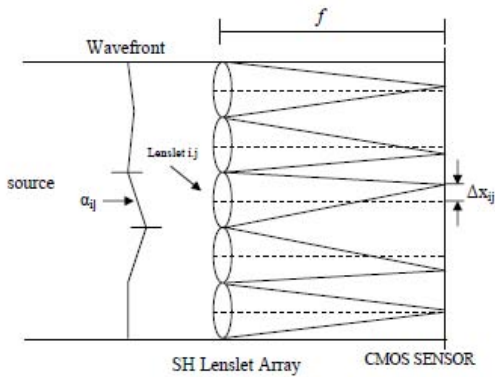


Figure 2 – SH WFS schematic (reproduced in Ref.[1])

Classical Control in Adaptive Optics

The control computer determines mirror commands from Shack-Hartmann wavefront sensor measurements using the influence, or poke matrix. Each individual actuator is “poked,” or sent a maximum or near-maximum voltage, while all other actuators are held at zero. The slope measurements corresponding to each poked actuator form the columns of the poke matrix. The sensor-command relationship is:

$$\mathbf{y} = \mathbf{\Gamma} \mathbf{c} \quad (1)$$

where \mathbf{y} is the vector of sensor outputs (both x and y measurements for each lenslet), $\mathbf{\Gamma}$ is the poke matrix, and \mathbf{c} is the DM command vector. A calibration process prior to the experiment determines the poke matrix. Once the matrix is known, the necessary DM commands can be obtained from a vector of sensor outputs by using the pseudoinverse, $\mathbf{\Gamma}^\dagger$, of the poke matrix. Since there are usually more sensor measurements than DM actuators, this forms the least squares solution to the correction problem.

Often in adaptive optics systems it is desirable to reconstruct the wavefront phase from the slope information. However, this paper is more concerned with determining the control to be applied to improve the wavefront than with knowing what the wavefront actually looks like. Also, since knowledge of the wavefront shape is not necessary for this reconstruction method, additional computation time is saved. Therefore, the poke matrix in this case may be referred to as the “reconstructor” in lieu of having an actual wavefront reconstruction step in the process.

Once the poke matrix has been determined, a classical integral controller is written in the form:

$$\mathbf{c}_{\text{new}} = \mathbf{c}_{\text{old}} - g \mathbf{\Gamma}^\dagger \mathbf{y} \quad (2)$$

where g is the integral gain. This controller will be augmented using adaptive filters as described in Section 2. Adaptive filters are desirable in adaptive optics as opposed to or in addition to fixed-gain reconstructor algorithms due to the rapidly changing nature of atmospheric turbulence. Adaptive filters vary the gains or filter weights as time progresses to better correct for varying parameters. To avoid confusion, it should be noted that adaptive control refers to the updating of gains in the correction algorithm, while adaptive optics refers to the presence of a component in the system that corrects by adapting, or varying, the beam’s optical path length.

2. ADAPTIVE FILTER

The NPS began research in adaptive filters for use in the control of optical beam jitter in space applications. Current research efforts include jitter control in high energy laser systems for maritime applications as well.

Adaptive filters can be infinite impulse response (IIR) or finite impulse response (FIR). IIR filters respond indefinitely because they contain internal feedback, yet for the same reason they can become unstable [8]. The response of an FIR filter dies off after a finite duration, and the filter itself is inherently stable. The filter used here is an FIR filter. Two commonly used implementations of an FIR filter include transverse and lattice. The simpler transverse implementation will be described here. An L^{th} order transverse FIR adaptive filter has the structure shown in Figure 3. Each of the L stages, or taps, delays the input signal by one unit, which leads many to call this filter a tapped-delay line. The filter output is expressed as follows:

$$y(n) = \sum_{i=0}^L w_i(n) x(n-i) = \mathbf{w}^T(n) \mathbf{x}(n) \quad (3)$$

where $\mathbf{w}(n)$ is the filter weight vector of length $L+1$ whose i^{th} component is $w_i(n)$, $\mathbf{x}(n)$ is the vector of delayed inputs $x(n-i)$, and $y(n)$ is the filter output.

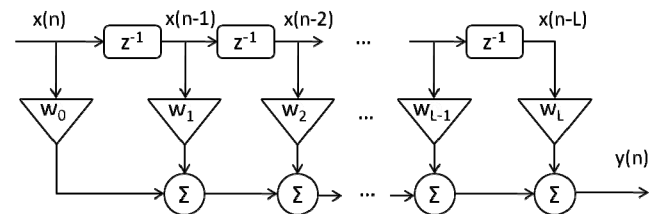


Figure 3 – Transverse FIR adaptive filter structure

Least Mean Square (LMS) Adaptive Filter

Figure 4 shows the simplest implementation of an adaptive algorithm. The objective here is to minimize the error $e(n)$, the difference between filter output $y(n)$ and a desired response or disturbance, $d(n)$:

$$e(n) = d(n) - \mathbf{w}^T(n)\mathbf{x}(n) . \quad (4)$$

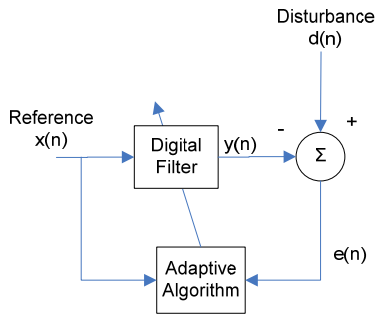


Figure 4 – Implementation of adaptive filter

When the statistics of the disturbance and the reference signal are available, the weights that minimize the mean square error (MSE), expectation of $e(n)^2$, can be computed. However, such information is often not available a priori in practice. In the Least Mean Square (LMS) adaptive filter developed by Widrow [9], the instantaneous squared error is minimized instead of MSE by a steepest gradient descent method updating the weights in the direction of lower error. The standard form of the LMS algorithm is given as follows,

$$\mathbf{w}(n+1) = \mathbf{w}(n) + \alpha \mathbf{x}(n)e(n) \quad (5)$$

where α is the adaptation rate.

The LMS method can be made more practical by a “Filtered-x” technique discussed by Widrow [9] and Kuo [10]. The filtered-x method accounts for the reality that a control signal must pass through a physical actuator before the result is sensed at the error sensor. The secondary plant contains information on the interaction between sensor and actuator, and its effect on the control action must be taken into account for improving performance and preventing instability in the system. Figure 5 shows an adaptive system with an I^{th} order filter, W , followed by the secondary plant transfer function, $S(z)$.

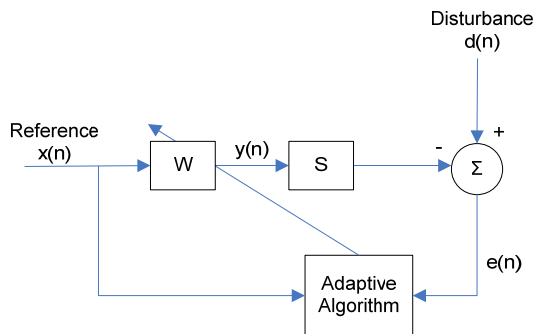


Figure 5 – Adaptive filter shown with secondary plant as in a real system

It is shown in Kuo [12] that in using the steepest gradient descent LMS algorithm when a secondary plant is present, the reference must be filtered by an estimate of this plant, $\hat{S}(z)$, before the reference is fed to the adaptive algorithm so that the adaptive filter produces a command that cancels the disturbance after, and not before, going through the secondary path dynamics. The final form of the system including the secondary plant is as shown in Figure 6. In practice, $S(z)$ may include system interactions that are difficult to model precisely, and the adaptive algorithm can compensate these modeling uncertainties in $\hat{S}(z)$ if the modeling error is not too large.

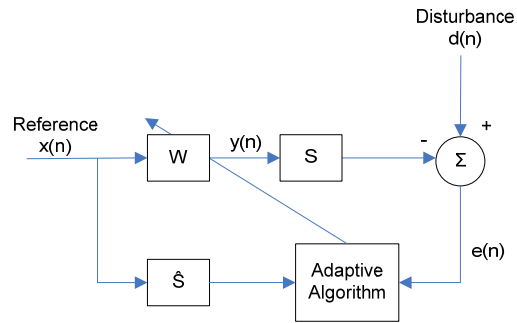


Figure 6 – Final system accounting for secondary plant

In the adaptive optics control problem, an external reference correlated to the disturbance is not available. Following the development by Kuo in [10], an internal reference, $r(n)$, which is an estimate of the disturbance, is generated by removing the effect of the adaptive filter output on the error as shown in Figure 7. If the model is precise, the reference signal becomes the disturbance itself.

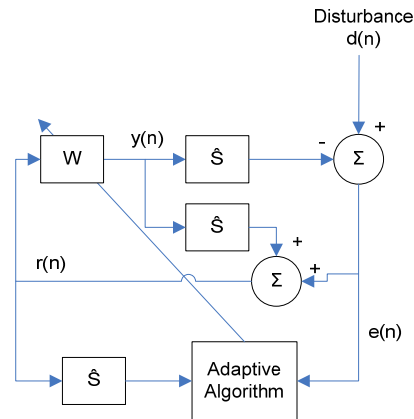


Figure 7 – Adaptive controller diagram with internally generated reference

Since obtaining a reference signal from the error forms a feedback path for the adaptive filter, it is called a feedback adaptive filter. Once all weights are converged, the adaptive system behaves as a Linear Time Invariant (LTI) system and therefore it is subject to the fundamental limitation of

feedback systems known as the Bode's integral theorem, or the waterbed effect. In addition, because there is a delay in estimating the disturbance, the ability of a true feedforward controller to address broadband disturbances is now limited. Feedback adaptive filters are most effective in addressing periodic, or narrowband disturbances. Adaptive filters also have difficulty when addressing constant bias without certain modifications [11].

In order to overcome these limitations, the adaptive controller is often placed in parallel with a classical controller, such as Proportional-Integral (PI) controller. Figure 8 shows some of the possible configurations of such a controller. The adaptive filter is denoted as $A(z)$ and the PI controller is denoted as $C(z)$. There is assumed to be a delay in the system represented by z^{-q} , and $\hat{S}(z)$ is the model of the secondary path. The path from the error to the adaptive filter is omitted for a clearer view of the diagram, as it is not critical for the issues discussed here.

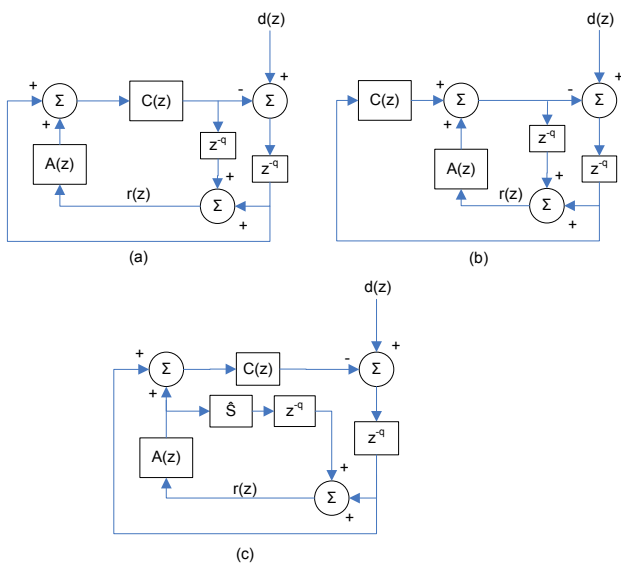


Figure 8 – (a) Adaptive filter output applied before PI, (b) Adaptive filter output applied after PI, (c) Decoupling of PI and AF loops

The diagram in (a) applies the output of the adaptive filter before the PI controller, and the secondary path transfer function at steady state in this case is given by the transfer function of the closed PI loop.

$$\hat{S}(z) = \frac{C(z)}{1 + z^{-q}C(z)} \quad (6)$$

Note that the secondary path is from the point the adaptive filter output is applied to the point the disturbance is added. In this configuration, the adaptive filter weights will not converge if the disturbance contains a DC component, or a bias, and it will have some oscillation at steady state

unless the bias is cancelled by the adaptive filter by accident. In general, the FIR filter is not capable of producing a bias output unless the input contains a bias component, and it cannot produce bias free output unless the input is a bias free signal. Although the PI control loop is supposed to remove the bias component in the loop, the adaptive filter and PI controller interact adversely and result in a residual error. More detailed analysis of this issue is given by Yoon, *et. al.*, in [11], and a solution for the problem called bias integration is presented, which will be applied to the controller in this study.

In the case of (b), the secondary path model becomes the sensitivity transfer function of the PI control loop as shown below.

$$\hat{S}(z) = \frac{1}{1 + z^{-q}C(z)} \quad (7)$$

Since the transfer function eliminates any DC component, the adaptive filter produces only no-bias component in the error. Meanwhile, the PI controller eliminates any remaining bias component in the error. The sensitivity transfer function, however, has significant attenuation in the lower frequencies as well and the effective gain of the adaptive filter in the low frequency range becomes very small, possibly leading to slower convergence.

For case (c), the secondary path is the same as in (a), but the reference signal is generated using only the output of the adaptive filter, which effectively decouples the adaptive filter and the PI controller feedback loops so that they do not interact. The reference signal in this case is given by:

$$r(z) = \frac{z^{-q}}{1 + z^{-q}C(z)} d(z) \quad (8)$$

As can be seen in Eq. (8), any bias component in the disturbance will be eliminated by the transfer function applied to the reference signal. Diagram (a), on the other hand, removes the effect of both controllers from the error and $r(z)$ becomes the estimate of $d(z)$, which includes the bias and causes adverse interaction between the adaptive filter and the PI controller. Gibson has implemented the feedback adaptive filter in the (c) configuration successfully in [5] and [6].

Multichannel LMS Adaptive Filter

Since an AO system is a Multi-Input and Multi-Output (MIMO) system, the LMS adaptive algorithm needs to be extended for use with multiple channels. Discussion of multichannel LMS can be found in Elliot, *et. al.* [12], Edwards [13], and Kuo [10]. For a multichannel adaptive filter, the number of reference signals can be independent of the number of the sensors or actuators. For M error sensors, K control actuators and J reference signals, there are $M \times K$

secondary path models and $K \times J$ weight vectors. Each secondary path model represents the relationship between the control action by the k^{th} actuator and the error observed by the m^{th} sensor. The command for the k^{th} actuator is generated combining all reference signals with weight vectors as shown below.

$$y_k(n) = \sum_{j=1}^J y_{kj}(n) = \sum_{j=1}^J \mathbf{w}_{kj}^T(n) \mathbf{r}_j(n) \quad (9)$$

The formula for updating the weight vector \mathbf{w}_{kj} is given as follows based on the steepest gradient descent method,

$$\mathbf{w}_{kj}(n+1) = \mathbf{w}_{kj}(n) + \alpha \sum_{m=1}^M \mathbf{x}_{jkm}(n) e_m(n), \quad (10)$$

where α is the adaptation rate and $\mathbf{x}_{jkm}(n)$ is $\mathbf{r}_j(n)$ filtered by the secondary path $S_{mk}(z)$. Assuming a rigid deformable mirror, meaning that mirror dynamics can be ignored, the secondary plant reduces to the dynamics of any control loop in the system and the mirror's poke matrix.

For a multichannel adaptive filter, the error can be taken either in actuator space or in sensor space and any number equal to or smaller than M can be the number of error signals to be used in the weight update. Similarly, the reference signal can be generated either in actuator space or sensor space. There is no restriction on the number of reference signals J . The secondary path model \hat{S}_{mk} is determined by the transfer function from the point where the actuator action is applied to the point before the disturbance is applied.

Sensor Space Error LMS

Suppose there is a poke matrix between the PI controller and the disturbance in (a) of Fig. 8. For the error measured by all M sensors, the secondary path is written as

$$S_{mk}(z) = \frac{C(z)}{1+z^{-q}C(z)} \Gamma_{mk} \quad (11)$$

and the filtered reference is written as:

$$\mathbf{x}_{jkm}(z) = S_{mk}(z) \mathbf{r}_j(z) = \frac{C(z)}{1+z^{-q}C(z)} \Gamma_{mk} \mathbf{r}_j(z) \quad (12)$$

Let

$$\mathbf{x}'_j(z) = \frac{C(z)}{1+z^{-q}C(z)} \mathbf{r}_j(z) \quad (13)$$

and the summation term on the right hand side of Eq. (10) can be written as:

$$\sum_{m=1}^M \mathbf{x}_{jkm}(n) e_m(n) = \sum_{m=1}^M \Gamma_{mk} \mathbf{x}'_j(n) e_m(n) = \mathbf{x}'_j(n) \sum_{m=1}^M \Gamma_{km}^T e_m(n) \quad (14)$$

Letting $\mathbf{e}'(n) = \Gamma^T \mathbf{e}(n)$, the converted error vector is of length K and an alternative expression of the weight update equation can be obtained as follows:

$$\mathbf{w}_{kj}(n+1) = \mathbf{w}_{kj}(n) + \alpha \mathbf{x}'_j(n) e'_k(n) \quad (15)$$

This form has a slight advantage in implementation in the Simulink environment.

Actuator Space Error LMS

If the error is measured in actuator space after applying the matrix Γ^\dagger , the matrix relating the actuator input to the measured error is $\Gamma^\dagger \Gamma$. The formulation of LMS can be obtained by replacing Γ by $\Gamma^\dagger \Gamma$ in Eqs. (11), (12), and (14). Since $\Gamma^\dagger \Gamma$ is an identity matrix by definition of Γ^\dagger , the converted error becomes $\mathbf{e}'(n) = \mathbf{e}(n)$ and Eq. (15) can be rewritten as:

$$\mathbf{w}_{kj}(n+1) = \mathbf{w}_{kj}(n) + \alpha \mathbf{x}'_j(n) e_k(n) \quad (16)$$

If the reference signal is also obtained in actuator space, the computation of the FIR filter and weight update can be reduced by decoupling all channels, *i.e.*, using only \mathbf{x}_k and $e_k(z)$ for generating the k^{th} actuator command. This is because the actuator action of one channel does not affect the error in the other channels and the reference signal to generate the canceling signal for a particular channel can be obtained from the error solely from that channel. This is equivalent to setting $\mathbf{w}_{kj}(n) = 0$ for all $j \neq k$ in Eq. (9) and computing Eq. (16) only for $\mathbf{w}_{kk}(n)$.

For this decoupled channel LMS, the adaptation rate needs to be set separately for each channel because of the difference in the error levels between the channels. Otherwise, the adaptation rate needs to be set very conservatively to account for the channel with largest disturbance, and the convergence of channels with small disturbances becomes very slow. In the coupled multichannel case, all reference signals are combined for all channels, which has an averaging effect on the error level differences among the channels.

Another way to approach this issue is to normalize the reference signal by the following formula,

$$\mathbf{x}''_j(z) = \frac{\mathbf{x}'_j(z)}{(\mathbf{x}'_j{}^T(z) \mathbf{x}'_j(z)) + \varepsilon} \quad (17)$$

and replace $\mathbf{x}'_j(n)$ in Eqs. (15) and (16) with $\mathbf{x}''_j(n)$. Here, ε is a small number to avoid dividing by zero. Normalization requires more computation but it can prevent

the controller from becoming unstable in cases of disturbance magnitude change.

Bias Integration

As mentioned before, the configuration in (a) of Fig. 8 cannot handle a constant bias. Yoon, *et. al.* introduced a technique called bias integration to modify the LMS algorithm to address constant bias for a Single Input Single Output (SISO) system [11]. In this study, the bias integration is extended for a multichannel case.

Following the bias integration method for the SISO case, each weight vector $\mathbf{w}_{kj}(n)$ of length L is augmented by a bias weight w_{jkb} , which is a constant scalar, to obtain an $L+1$ length vector $\tilde{\mathbf{w}}_{kj}(n)$ as follows:

$$\tilde{\mathbf{w}}_{kj}(n) = [w_{kj1}(n) \quad \cdots \quad w_{kjL}(n) \quad w_{jkb}]^T \quad (18)$$

The reference signal and filtered reference signal vectors are similarly augmented by bias terms:

$$\tilde{\mathbf{r}}_j(n) = [r_{j1}(n) \quad \cdots \quad r_{jL}(n) \quad r_{jkb}]^T \quad (19)$$

$$\tilde{\mathbf{x}}_{jkm}(n) = [x_{jkm1}(n) \quad \cdots \quad x_{jkmL}(n) \quad x_{jkmkb}]^T \quad (20)$$

where r_{jkb} is a constant and x_{jkmkb} is given as

$$x_{jkmkb}(z) = S_{mk}(z)r_{jkb}(z). \quad (21)$$

Similarly, x'_{jkb} is the filtered r_{jkb} defined as follows:

$$x'_{jkb}(z) = \frac{C(z)}{1+z^{-q}C(z)}r_{jkb}(z) \quad (22)$$

At steady state, x'_{jkb} is r_{jkb} multiplied by the DC gain of the secondary path transfer function and the adjustment of the bias weight by the secondary path DC gain described in Yoon, *et. al.*, [11], is no longer necessary.

Now the output of the filter is given as:

$$\begin{aligned} \tilde{y}_k(n) &= \sum_{j=1}^J \tilde{\mathbf{w}}_{kj}^T(n)\tilde{\mathbf{r}}_j(n) \\ &= \sum_{j=1}^J \mathbf{w}_{kj}^T(n)\mathbf{r}_j(n) + \sum_{j=1}^J w_{jkb}(n)r_{jkb}(n) \end{aligned} \quad (23)$$

and the weight update can be written as follows:

$$\begin{aligned} \tilde{\mathbf{w}}_{kj}(n+1) &= [\mathbf{w}_{kj}(n+1), w_{jkb}(n+1)]^T \\ &= [\mathbf{w}_{kj}(n), w_{jkb}(n)]^T + \alpha [\mathbf{x}'_j{}^T(n), x'_{jkb}(n)]^T e'_k(n) \end{aligned} \quad (24)$$

The bias weight update can be written in terms of the sum of the bias weights as

$$\sum_{j=1}^J w_{jkb}(n+1) = \sum_{j=1}^J w_{jkb}(n) + \alpha e'_k(n) \sum_{j=1}^J x'_{jkb}(n), \quad (25)$$

and the sum of bias terms over j can be redefined as:

$$w_{kb}(n) = \sum_{j=1}^J w_{jkb}(n) \quad (26)$$

If the same constant is used for all reference signals, *i.e.*, $r_b(n) = r_{jkb}(n)$, then Eqs. (23) and (25) can be reduced to the following formulae:

$$\tilde{y}_k(n) = \sum_{j=1}^J \mathbf{w}_{kj}^T(n)\mathbf{r}_j(n) + r_b(n) \sum_{j=1}^J w_{jkb}(n) \quad (27)$$

$$= \sum_{j=1}^J \mathbf{w}_{kj}^T(n)\mathbf{r}_j(n) + r_b(n)w_{kb}(n)$$

$$w_{kb}(n+1) = w_{kb}(n) + \alpha e'_k(n)Jx'_b(n) \quad (28)$$

where $x'_b(n)$ is the filtered $r_b(n)$ obtained by Eq. (22). Simulation results using this method are presented in Section 5. The following two sections describe components in the experimental testbed.

3. TURBULENCE SIMULATOR

Air turbulence arises from the heating and cooling of the Earth's surface and causes changes in the index of refraction of the air. These changes alter the path of light propagating through the atmosphere. Atmospheric turbulence in a vertical path has been simulated successfully in adaptive optics for many years using the Kolmogorov turbulence theory. This theory is based on the assumptions that small scale turbulent motions are statistically homogeneous, isotropic, and independent of large-scale structure [14], [15]. Statistical variations of the atmosphere's index of refraction can then be described mathematically. Popular systems for simulating turbulence include rotating phase wheels imprinted with Kolmogorov atmospheric statistics [16], as well as liquid crystal spatial light modulators [17], [18].

Liquid Crystal (LC) Spatial Light Modulator (SLM)

The NPS is using LC SLMs from Holoeye with software developed by the Naval Research Laboratory in Albuquerque, NM. The Holoeye SLM is a π phase change device that can be modified to 2π or higher by Fourier filtering to choose the appropriate diffractive order to propagate through the system. Both NPS and NRL are

using the LC2002, shown in Figure 9 on the left and mounted on the NPS optical table on the right. Development of a turbulence simulator using one SLM is described by Wilcox, et al. in a recent paper [19].

The NRL-developed software allows the user to specify telescope and site parameters such as telescope diameter, D , and the atmospheric coherence length, r_0 . Turbulence generation can be performed with either the Zernike polynomial expansion or the Karhunen-Loève polynomial expansion. Statistical calculations of Zernike-Kolmogorov residual errors from Fried [20] and Noll [21] are used to determine the Zernike coefficients for generating phase screens. The Karhunen-Loève (K-L) modes are a linear combination of Zernike modes and are useful in describing propagation through a random medium such as the atmosphere.

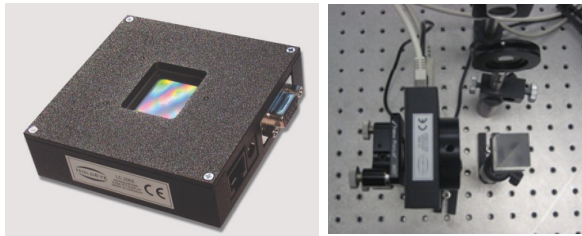


Figure 9 – Holoeye SLM, LC2002

Once site parameters, a mode set, and any initial calibration aberrations are selected, the controller generates a user-specified number of phase screens which are splined together to provide continuous transition between each instance of turbulence. This splining technique is described by Wilcox in [19]. The smoothed turbulence profile is then applied to the SLM for atmospheric simulation.

Thick Aberrator Simulation

In vertical turbulence, it is often assumed that the atmosphere is composed of several thin layers at various distances from the telescope. These distances can be measured. Ideally, each of these layers would be conjugate to a correction system, though hardware, financial, and other technical concerns make multi-conjugate AO systems difficult to implement. However, in horizontal atmosphere which cannot be described or measured in the same way as vertical atmosphere, the locations of multiple “layers” are difficult to determine. A thick aberrator to approximate the effects of horizontal turbulence will be simulated in the laboratory using two SLMs placed in the optical path. As only one WFS-DM combination is available, only one SLM (seen second in the optical path) will be conjugate to the WFS-DM pupil plane and its effect expressly corrected for. However, the effect of the other SLM (seen first in the optical path) will be to create additional turbulence that propagates through the system and helps to simulate the thick turbulence layer. At this time, no accounting for branch points in the atmospheric phase profile is included. The next step in the experiment will be to move the second SLM to various distances out of the pupil to determine how

well the adaptive optics system performs. This will lend insight into thick aberrator performance that will be useful in future experiments, when it is desirable to correct for other pupil planes whose locations will not be as well known as the current system pupil. This will provide information on the best control techniques to use in such an environment. Experiments in a vertical propagation path with the DM out of pupil have been performed at the Starfire Optical Range [22].

4. LABORATORY TESTBED

The NPS has built an adaptive optics system to be incorporated in the future with the existing High Energy Laser (HEL) testbed currently undergoing research on jitter control for shipboard applications. For initial experiments, it is assumed that tip and tilt will be removed by the jitter control part of the testbed. As such, the AO system will only correct for the higher order aberrations due to atmospheric turbulence. The complete AO system is shown in Figure 10. The beam paths and primary components are described below.

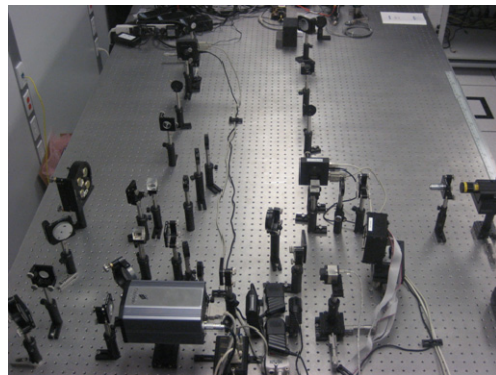


Figure 10 – NPS AO system

Beam Paths

A microscope objective and lens expand and collimate the sources laser beam, which is then split by a beamsplitter to follow two paths. One beam travels through the aberrator provided by the two SLMs and accompanying optics, as shown in Figure 11. As described in Section 3, the SLM is an LC2002 from Holoeye Corp. The device is capable of operating at up to 30 Hz. The aberrator path consists of the first SLM immediately followed by an afocal lens system which relays the SLM profile to a pupil plane (which will not be specifically corrected for without a second DM-WFS combination). An iris is used to Fourier filter the device and allow one of the first diffractive orders to pass through, achieving a 2π or full wave range of aberration. The beam then passes through the second SLM, immediately followed by another Fourier filter and an afocal system that relays the SLM profile to the tip/tilt mirror (currently being used as a simple flat). This mirror is conjugate to the DM and SH WFS.

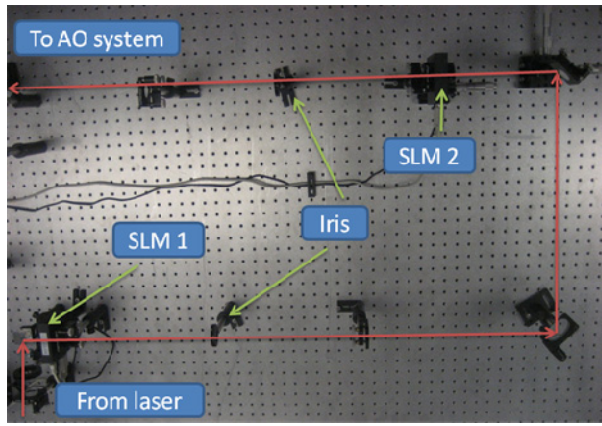


Figure 11 – Aberrator beam path

The second beam passing through the first beamsplitter serves as a reference that can take two additional paths. The first is a pure reference which bypasses the DM and is relayed to the SH WFS. This reference is what will be used to drive the control system. The second path, while still bypassing the aberrator, is relayed to the DM before reaching the SH WFS, and will be referred to as the “DM path.” This path is used to generate the poke matrix or influence function of the DM. While the beam in this path is “unaberrated” since it does not travel through the aberrator path, it will include aberrations from the surface of the DM itself as well as any introduced by the additional optical surfaces. Alternatively, an unaberrated DM beam can be formed by using the aberrator path while placing no aberrations on the SLM devices. However, this path contains more optical surfaces which can introduce additional aberrations. The reference and DM beam paths are shown in Figure 12 and Figure 13, respectively.

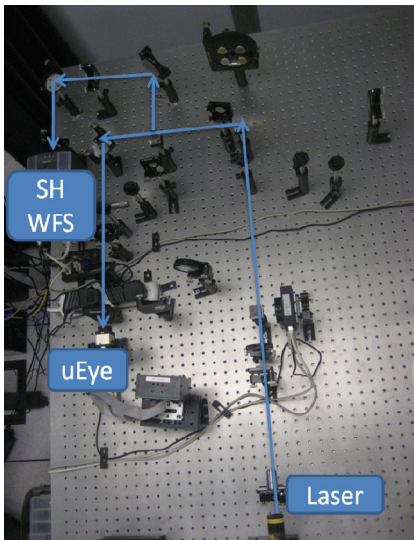


Figure 12 – Reference path

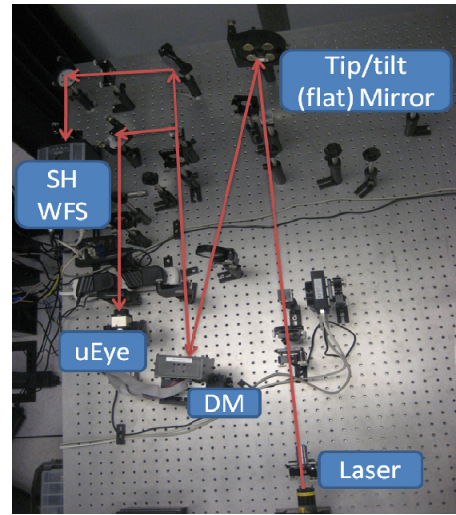


Figure 13 – DM path (unaberrated)

Primary Optical Table Components

The laser used is a CVI Melles Griot HeNe Class II laser with output power of 0.5 mW cw, operating at a wavelength of 633 nm. The deformable mirror is a 59-channel Flexible Optical BV (OKO) Micromachined Membrane Deformable Mirror (MMDM). The membrane mirror is mounted across a two-dimensional array of electrodes which change the mirror’s shape according to the control voltages applied [23]. The actuator geometry is shown in Figure 14. The control signals, \mathbf{c} , calculated by the control law fall between ± 1 and are then translated into 8-bit values between 0 and 255 to be applied as voltages to the mirror. The mirror surface deflection depends linearly on the square of the applied voltage. The relationship between control signals and voltage commands is as follows:

$$\mathbf{V}_{MMDM} = (0.5(\mathbf{c} + 1))^{1/2} (255) \quad (29)$$

where \mathbf{c} is the vector of calculated control signals and \mathbf{V} is the vector of voltage commands sent to the mirror.

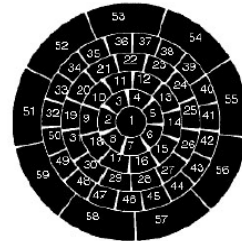


Figure 14 – Actuator geometry, 59-ch OKO MMDM²²

The wavefront sensor is a Shack-Hartmann array of 127 lenslets arranged in a hexagonal pattern. The array is attached directly to a Roper Scientific Cascade 128+ camera with a resolution of 128 x 128 pixels and a 16-bit frame rate of 500 fps. The science camera is an IDS uEye-2210SE CCD camera with a resolution of 640 x 480 pixels and an 8-bit frame rate of 75 fps. It is used to capture the point

spread functions (PSFs) of the corrected and uncorrected spots.

Two computer controllers are used for the full experimental system. All elements of the adaptive optics control system itself are driven by one computer, while the aberrator elements (SLMs) and uEye science camera are controlled separately. Simulations are run in Matlab’s Simulink environment, while the optical table elements are currently driven using Matlab only. Future work will include transitioning AO table control to Simulink as well.

The SLMs are controlled using NRL software developed as a Matlab graphical user interface (GUI), described in more detail in Section 3. Figure 15 shows the control monitors. Each SLM is currently run from a separate GUI. The top two monitors show the phase screens applied to each SLM. The bottom left screen shows the two GUIs, and the bottom right screen displays the uEye science camera image.

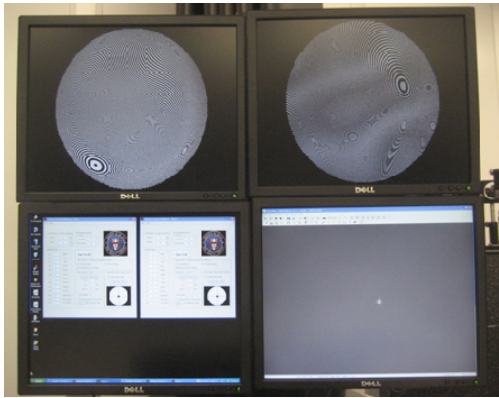


Figure 15 – SLM and science camera control screens

5. SIMULATION

In this section, adaptive control algorithms to be applied in the AO testbed described in the previous section are investigated by numerical simulations performed in the MATLAB/Simulink environment. Figure 16 shows the implementation of the adaptive and classical loops with a more detailed breakdown of the secondary path.

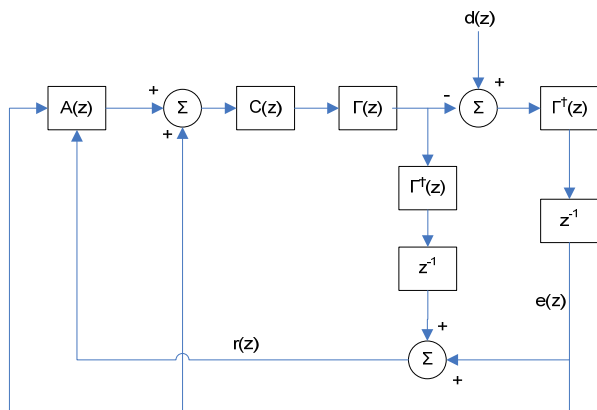


Figure 16 – Simulation diagram showing breakdown of secondary path and location of disturbance injection

The poke matrix used in simulation was generated from the new testbed using the 59-channel OKO MMDM described in the previous section. Its dimensions are 224 x 59, as only 112 of the 127 SH WFS lenslets are seen by the WFS camera. The simulation model is constructed entirely in discrete-time with a sample frequency of 100 Hz. The delay in the system, q , is set to 1.

The disturbance is injected in sensor space (after the poke matrix) as that is where its effect is seen in a real system. The disturbance is a combination of three sinusoids and a band-limited white noise with bias. The power of the white noise is 1.0E-10 and the bias is set to 0.2. The frequencies of the disturbance are selected so that their periods are not related, and that they are well within the frequency range where the secondary path has sufficient gain. The disturbance applied to each sensor output is identical.

Controller Design

The classical control loop has a proportional and integral (PI) controller given as follows.

$$C(z) = \frac{K_i z}{z - 1} + K_p \quad (30)$$

The integral gain, K_i , and proportional gain, K_p , are designed to meet reasonable specifications of the PI control loop. Their values are 0.315 and 0.135, respectively, and the -3dB bandwidth of the closed loop transfer function of this controller is about 5.4 Hz. The rise time is 0.06 sec.

The adaptive filter used here is a normalized adaptive filter described in Section 2 with the bias integration. It is applied in parallel with the PI controller loop in the (a) configuration shown in Figure 8. The 59-channel error observed in actuator space and 59-channel reference signal generated from actuator space error are used for the adaptive filter.

Simulation Results

The disturbance frequencies are 12.5 Hz, 8.2 Hz, and 1.0 Hz, with phases chosen randomly as 2.98 rad, 1.37 rad, and 0 rad, respectively. The power of the band-limited white noise is $1.0 \cdot 10^{-10}$ and a constant bias of 0.2 is applied to all sensor space channels. A gain of $10^{-4}/60$ was applied to the overall disturbance for scaling of the error level. The frequency spectrum of the disturbance is shown in Figure 17.

Figure 18 shows the steady state actuator error when only the PI control is applied. Steady state data is obtained from 10 sec to 20 sec where the adaptive filter is very well converged. All channels are plotted. It can be seen that PI controller provides some attenuation of the error up to 10 Hz, but fails to eliminate the deterministic periodic components. Figure 19 shows the frequency spectrum of the actuator space error with the adaptive filter applied.

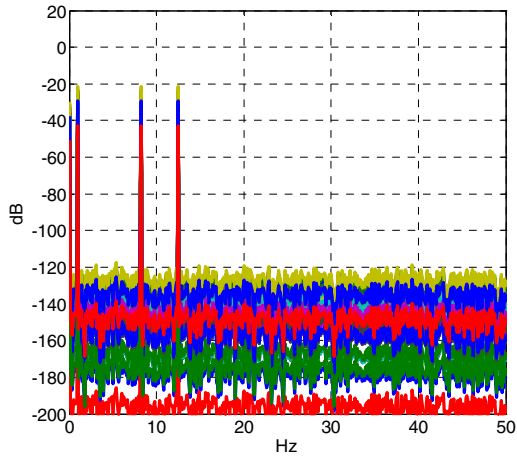


Figure 17 – Disturbance frequency spectra of all channels in actuator space

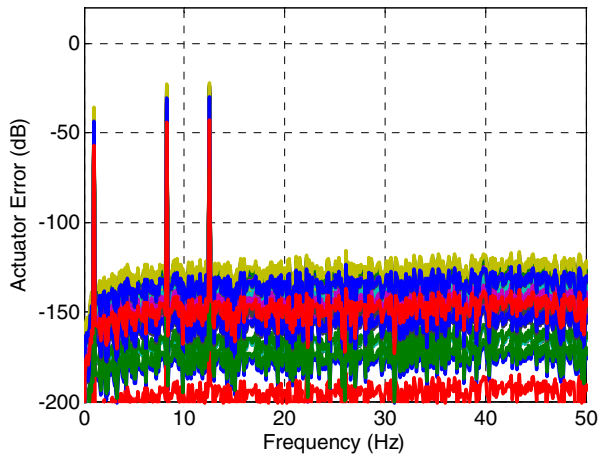


Figure 18 – Frequency spectra of actuator space error in all channels with PI control and without adaptive filter

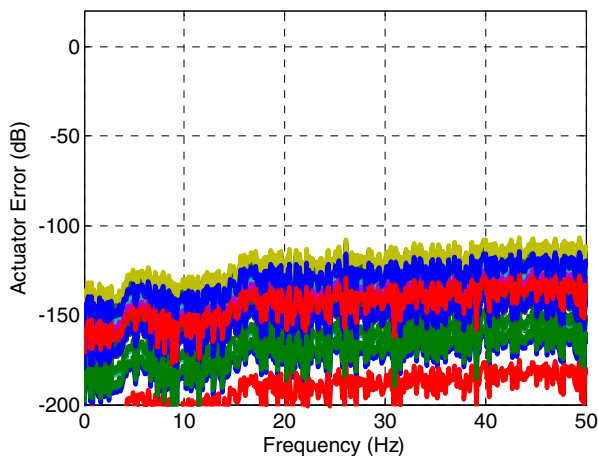


Figure 19 – Frequency spectra of actuator space error in all channels with normalized adaptive filter with bias integration

The number of weights for each adaptive filter is 16, including one bias weight. The adaptation rate and bias constant are 0.02 and 0.2, respectively. As can be seen, the three deterministic frequency components are completely eliminated. A slight error increase above 15 Hz indicates that the feedback adaptive controller is still subject to the waterbed effect. Figure 20 shows the convergence of all actuator space errors in linear scale. Figure 21 is a log scale plot to show the Root Mean Square (RMS) of the actuator space error computed over all channels and divided by the RMS of the disturbance, which is the square root of the sum of the squares over all channels averaged for 20 sec.

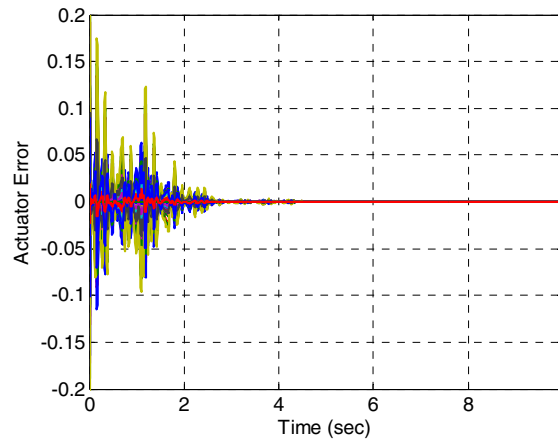


Figure 20 – Convergence of errors in actuator space with normalized adaptive filter with bias integration

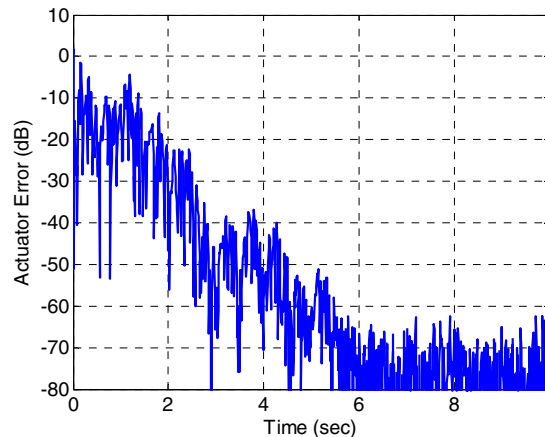


Figure 21 – Convergence of normalized root mean square error of all channels in actuator space with normalized adaptive filter with bias integration

Figure 22 shows the 15 filter weights of Channel 1 as an example of the convergence behavior of the weights. Figure 23 shows the bias weights of all channels. The appropriate number of weights depends on the disturbance characteristics; in this simulation, 14-16 weights produced good convergence with stable adaptation rates. Simulated disturbances more representative of an adaptive optics scenario can be found in [24] and [25], and a disturbance

that closely resembles the disturbance profile expected in the actual environment will be tested in the future.

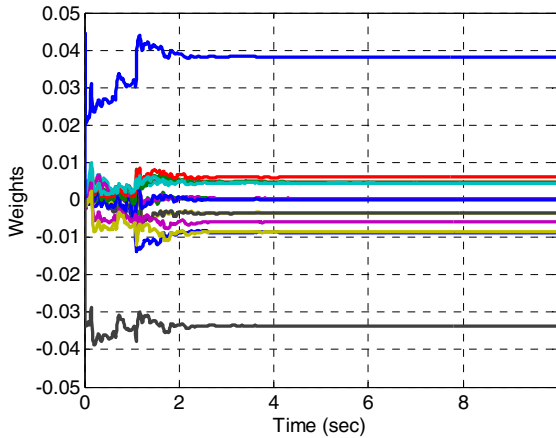


Figure 22 – Example of weight convergence excluding bias weight

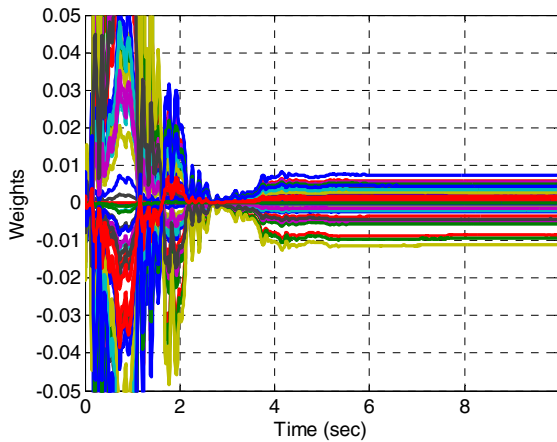


Figure 23 – Convergence of bias weights for all channels

To illustrate the benefit of bias integration, simulation of an adaptive filter without bias integration was conducted. The convergence of actuator space error is shown in Figure 24.

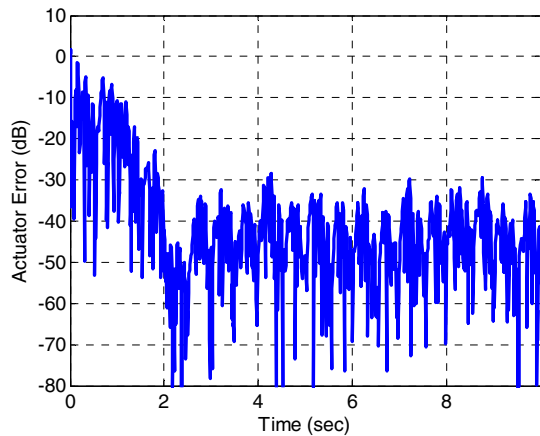


Figure 24 – Convergence of normalized root mean square error of all channels in actuator space with adaptive control without bias integration

The convergence of the weights and the frequency spectra of the error at steady state are shown in Figures 25 and 26, respectively. As can be seen, the weights oscillate at steady state. While the periodic component peaks are attenuated, overall error is increased.

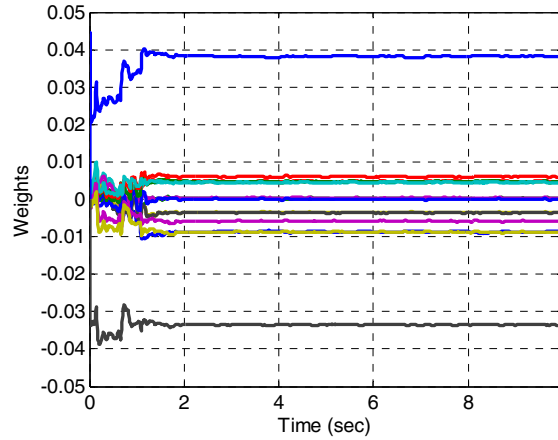


Figure 25 – Convergence of one set of weights without bias integration

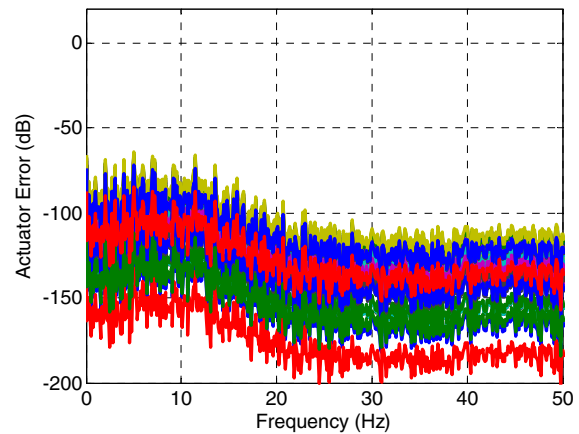


Figure 26 – Frequency spectra of actuator space error in all channels with normalized actuator space adaptive filter without bias integration

6. CONCLUSIONS

This paper has described a newly developed laboratory testbed to investigate advanced beam control methods for adaptive optics in the presence of a thick aberrator for a maritime environment. Simulation has been conducted on the normalized, actuator space, multichannel LMS adaptive filter with bias integration. The results demonstrate the effectiveness of the method in the presence of a bias component in the disturbance. Sensor space error LMS was also performed for comparison, and it verified that although it uses more error information than actuator space LMS, it does not produce better results. This was expected because the actuators can only affect a subspace of the sensor space, and minimizing sensor space error in the square error sense

is equivalent to eliminating all errors in actuator space. It was also found that sensor space LMS has slower convergence.

The actuator space LMS method employed here uses the errors and references of all channels in updating the weight vector for each channel. The decoupled actuator space LMS method requires only one error and reference for updating a weight vector for one channel, and computation can be reduced. Simulations were performed, and the results show that the decoupled LMS has slightly faster convergence. However, it may be more practical to use the full multichannel LMS in a situation where the poke matrix estimate is not accurate. In such a case, the effect of the control action of one actuator is no longer contained in one channel but spread in other channels, and full channel LMS is expected to be more robust.

Future work will include incorporating DM and WFS camera code into the Simulink model to drive the experimental system from Simulink. Additionally, the adaptive algorithms will be compared in the presence of a thick aberrator provided by the two-SLM system and while moving the second SLM in and out of pupil as described in Section 3. Comparisons will be made both in simulation and experiment to the performance of UCLA's multichannel lattice filter. In addition, the LMS algorithm will be compared to the Recursive Least Squares (RLS) algorithm. RLS is similar to LMS, but includes past data in the cost function by introducing a forgetting factor, which weights the most recent data the most heavily. This method converges faster than the LMS method and leads to smaller steady state error, but is more computationally intensive [10].

7. ACKNOWLEDGEMENTS

This work has been performed with funding from the Office of Naval Research and with significant technical assistance from the Naval Research Laboratory, Albuquerque, NM.

REFERENCES

- [1] M. R. Allen, "Wavefront Control for Space Telescope Applications Using Adaptive Optics," Master's Thesis, NPS, Monterey, CA, 2007.
- [2] D. C. Burtz, "Fine Surface Control of Flexible Space Mirrors Using Adaptive Optics and Robust Control," PhD Dissertation, NPS, Monterey, CA, 2009.
- [3] J.R. Watkins and B. N. Agrawal, "Use of Least Mean Squares Filter in Control of Optical Beam Jitter," AIAA Journal of Guidance, Control, and Dynamics, Vol. 30, No. 4, 2007.
- [4] M. J. Beerer, "Adaptive Filter Techniques for Optical Beam Jitter Control and Target Tracking," Master's Thesis, NPS, Monterey, CA, 2008.
- [5] T. A. Rhoadarmer, et. al., "Adaptive Control and Filtering for Closed-Loop Adaptive-Optical Wavefront Reconstruction," SPIE Advanced Wavefront Control: Methods, Devices, and Applications IV, Vol. 6306, No. 1, 2006.
- [6] Y.-T. Liu and J. S. Gibson, "Adaptive Control in Adaptive Optics for Directed-Energy Systems," Optical Engineering, Vol. 46, No. 4, 2007.
- [7] R. K. Tyson, Introduction to Adaptive Optics, SPIE Press, Bellingham, WA, 2000.
- [8] S. Haykin, Adaptive Filter Theory, Prentice-Hall, Inc., Upper Saddle River, NJ, 2002.
- [9] B. Widrow and S. D. Stearns, Adaptive Signal Processing, Prentice-Hall, Inc., Upper Saddle River, NJ, 1985.
- [10] S. M. Kuo and D. R. Morgan, Active Noise Control Systems, John Wiley & Sons, Inc., New York, NY, 1996.
- [11] H. Yoon, B. E. Bateman, and B. N. Agrawal, "Laser Beam Jitter Control Using Recursive-Least-Square Adaptive Filters," DEPS Beam Control Conference, 2008.
- [12] S. J. Elliott, I. M. Stothers, and P. A. Nelson, "A Multiple Error LMS Algorithm and Its Application to the Active Control of Sound and Vibration," IEEE Transactions on Acoustics, Speech, and Signal Processing, Vol. ASSP-35, No. 10, 1987.
- [13] S. G. Edwards, "Active Narrowband Disturbance Rejection on an Ultra Quiet Platform," PhD Dissertation, NPS, Monterey, CA, 1999.
- [14] M. C. Roggemann and B. Welsh, Imaging Through Turbulence, CRC Press, Inc., Boca Raton, FL, 1996.
- [15] L. C. Andrews, Field Guide to Atmospheric Optics, SPIE Press, Bellingham, WA, 2004.
- [16] S. V. Mantravadi, T. A. Rhoadarmer, and R. S. Glas, "Simple Laboratory System For Generating Well-Controlled Atmospheric-Like Turbulence," SPIE Advanced Wavefront Control: Methods, Devices, and Applications II, Vol. 5553, 2004.
- [17] M. K. Giles, et. al., "Setting Up A Liquid Crystal Phase Screen To Simulate Atmospheric Turbulence," SPIE High-Resolution Wavefront Control: Methods, Devices, and Applications II, Vol. 4124, 2000.

- [18] J. D. Schmidt, M. E. Goda, and B. D. Duncan, "Aberration Production Using A High-Resolution Liquid-Crystal Spatial Light Modulator," *Applied Optics*, Vol. 46., No. 13, 2007.
- [19] C. C. Wilcox, et. al., "Atmospheric Simulator For Testing Adaptive Optics Systems," *SPIE Advanced Wavefront Control: Methods, Devices, and Applications VI*, Vol. 7093, 2008.
- [20] D. L. Fried, "Statistics of a Geometric Representation of Wavefront Distortion," *J. Opt. Soc. Am.*, Vol. 55., No. 11, 1965.
- [21] R. J. Noll, "Zernike Polynomials and Atmospheric Turbulence," *J. Opt. Soc. Am.*, Vol. 66., No. 3, 1976.
- [22] M. Mateen, et. al., "Adaptive Optics with the Deformable Mirror Not In Pupil - Part 1: Experimental Results," *SPIE Advanced Wavefront Control: Methods, Devices, and Applications VI*, Vol. 7093, 2008.
- [23] *Adaptive Optics Guide*, OKO Technologies, Delft, Netherlands, 2008.
- [24] J. S. Gibson, C.-C. Chang, and B. L. Ellerbroek, "Adaptive Optics: Wave-front Correction by Use of Adaptive Filtering and Control," *Applied Optics*, Vol. 39, No. 16, 2000.
- [25] B. L. Ellerbroek and T. A. Rhoadarmer, "Real-time Adaptive Optimization of Wave-front Reconstruction Algorithms for Closed-loop Adaptive-optical Systems," *SPIE Adaptive Optical System Technologies*, Vol. 3353, 1998.

Research Laboratory at Hitachi, Ltd. from 2005 to 2009 conducting servo control research for Hard Disk Drives.

Brij Agrawal is currently a Distinguished Professor in the Department of Mechanical and Astronautical Engineering and Director of the Spacecraft Research and Design Center at the Naval Postgraduate School. He has developed research programs in acquisition, tracking, and pointing of flexible spacecraft with optical payloads; active vibration control, isolation, and suppression using smart structures; space robotics, satellite servicing, space system design, and computer aided design tools.



BIOGRAPHY

Melissa Corley is a PhD candidate at the Naval Postgraduate School in the Department of Mechanical and Astronautical Engineering. She earned a B.S. in mechanical engineering and an M.S. in aeronautics and astronautics from Stanford University in 2004. Her first Air Force assignment was as a developmental engineer at the Air Force Research Laboratory's Starfire Optical Range at Kirtland AFB, Albuquerque, NM.



Masaki Nagashima is a National Research Council (NRC) Research Associate and he has been with the Spacecraft Research and Design Center at the Naval Postgraduate School since June, 2009. He earned his B.S. and M.S. in mechanical engineering from Hokkaido University in 1994 and 1996, respectively. He earned another M.S. from Stanford University in 1997 and earned his doctoral degree in control theory from Columbia University in 2004. He worked for the Central

